



*Supplement of*

**Basin-scale gyres and mesoscale eddies in large lakes: a novel procedure for their detection and characterization, assessed in Lake Geneva**

**Seyed Mahmood Hamze-Ziabari et al.**

*Correspondence to:* Seyed Mahmood Hamze-Ziabari (mahmood.ziabari@epfl.ch)

The copyright of individual parts of the supplement might differ from the article licence.

**Table S1.** Summary of the measurement transects (T). The Swiss coordinate system is used ([SwissTopo](#)).

<b>Field campaign</b>	<b>Transect</b>	<b>Starting point (Easting, Northing)</b>	<b>Ending point (Easting, Northing)</b>	<b>Field duration</b>	<b>Number of measurement points</b>
21 September 2019	T2	(537524, 140687)	(537484, 149698)	1h 55m	10
21 September 2019	T2L	(535746, 140703)	(535678, 149702)	1h 59m	10
21 September 2019	T2R	(539874, 140691)	(539849, 149710)	2h 05m	10
22 September 2019	T2	(535746, 140703)	(537484, 149698)	2h 11m	10
22 September 2019	T2H	(528460, 146176)	(545498, 144617)	3h 17m	12
24 October 2019	T2	(535974, 140182)	(535926, 149197)	2h 01m	10
24 October 2019	T3	(522105, 136613)	(516003, 143554)	2h 17m	10
25 October 2019	T1	(550011, 139223)	(552114, 145753)	1h 42m	8
25 October 2019	T1H	(544996, 144517)	(554939, 141192)	2h 17m	8
25 November 2019	T1	(550690, 138496)	(550637, 146539)	1h 53m	9
25 November 2019	T2	(537197, 140678)	(535157, 149689)	2h 08m	10
25 November 2019	T3	(520675, 137339)	(520701, 144344)	1h 38m	8
3 September 2020	T6	(513241, 142532)	(516478, 139786)	2h 19m	Continuous
20 October 2020	T4	(525392, 138381)	(520668, 144837)	4h 43m	Continuous
20 October 2020	T5	(524640, 136585)	(522927, 140433)	1h 56m	Continuous

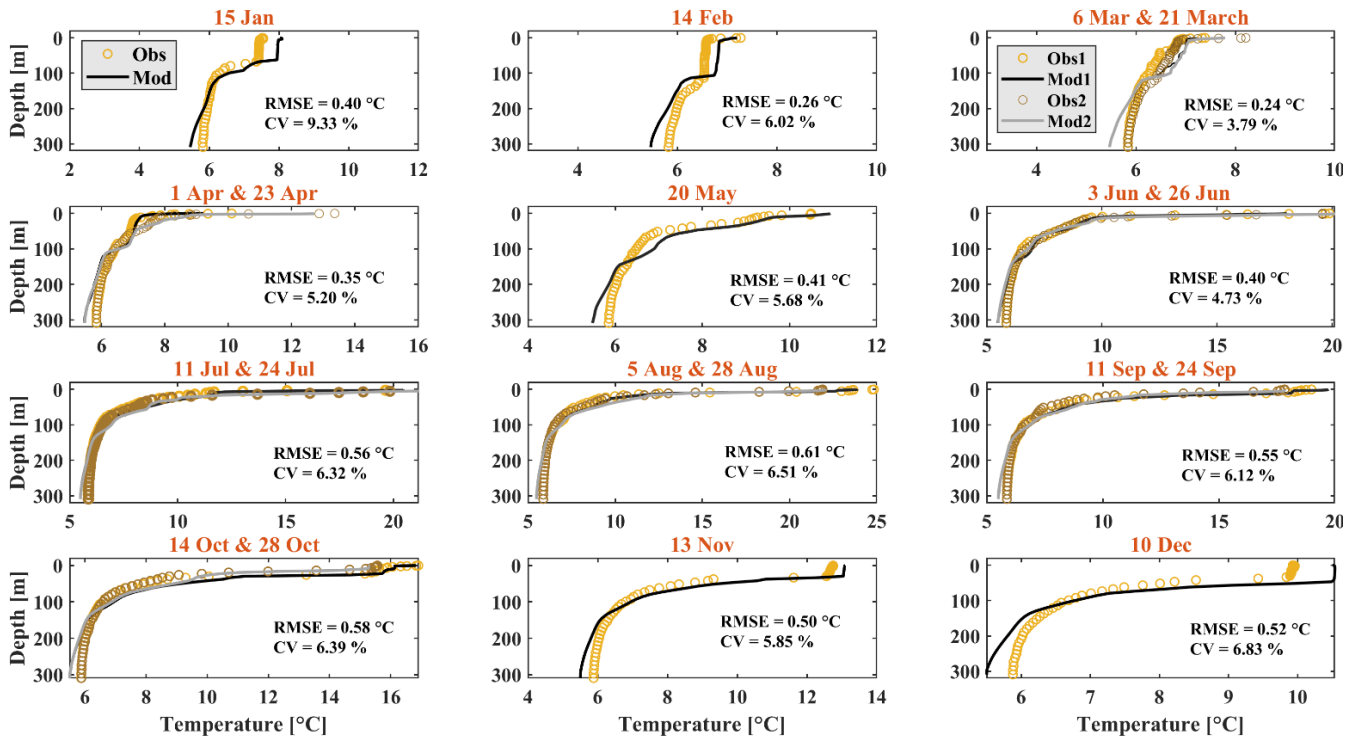


**Figure S1.** Comparison between observed (Orange: Obs1, Brown: Obs2; circles) and modeled (Mod1, Mod2: black lines; see legends) temperature profiles at the CIPEL SHL2 monitoring station (for location, see Fig. 1b) in Lake Geneva for 2019. RMSE indicates the Root-Mean Square Error (RMSE) between observed and modeled temperature profiles. The Coefficient of Variation (CV) is the ratio of RMSE to the average of values observed.

### S1. Synthetic Aperture Radar (SAR) imagery

The patterns observed in the SAR images are due to changes in the water surface roughness, which is influenced by wave/current interactions, natural surface films and spatial variations of the local wind field (Johannessen et al., 2005). Gyres or eddies that appear in SAR images as dark spiral features are called “black” or “classical” eddies (Karimova, 2012). These dark features are associated with surfactant films or slicks that suppress short wind waves and thus reduce radar backscatter (Yamaguchi and Kawamura, 2009). At higher wind speeds (5-6 m/s at 10 m), wind-induced mixing in the upper layer will dissipate/redistribute the surface slicks, thus preventing the damping mechanism induced by the presence of surfactants (Dokken and Wahl, 1996; Johannessen et al., 1996). On the other hand, for C-band SAR imagery, little differentiation in surface roughness is evident for wind speeds below  $3.25 \text{ ms}^{-1}$  (Donelan and Pierson, 1987; Johannessen et al., 1996). In summary, SAR imagery can reveal gyres (more generally, surface current fields) under light wind conditions where the water surface is partially covered by (natural) surfactants. These conditions exist on Lake Geneva.

20 Caution should be taken when interpreting SAR images, however, since dark zones can also be due to non-uniformity in the surface wind field, e.g., (i) small-scale inhomogeneities of the near-surface wind field, (ii) wind shade, (iii) atmospheric convection, and (iv) atmospheric gravity waves (Moran et al., 2002; Wang et al., 2019). Therefore, the available SAR imagery and selected images were analyzed based on the prevailing wind field, and then combined these images with in situ observations and numerical modeling. In total, 78 images for 2016-2019 were obtained from the European Space Agency (ESA) Sentinel-1A and Sentinel-1B satellites for Lake Geneva.

25 As mentioned in Section 3.2, SAR imagery can aid in the detection of gyre boundaries. For example, the boundaries between two cyclonic (counterclockwise) gyres at the eastern part of lake, i.e., CG1 and CG2, can be determined using SAR data obtained from Sentinel-1 on 19 July and 12 October 2018 (Figure 4). Comparisons between the OW values from numerical results and the patterns observed in the SAR images are shown in Figure 4, where two (elliptical) gyres are evident. The minor/major axes of gyres CG1 and CG2 are approximately 6.5/12.9 and 9.8/15.9 km, respectively. The Coriolis force plays an important role in the generation of these gyres, since their dimensions are much larger than the internal Rossby radius of deformation (Cushman-Roisin and Beckers, 2011). The typical range of the internal Rossby radius for Lake Geneva is  $O(5$  km) during the strongly stratified season and  $O(1$  km), during the weakly stratified season (Lemmin and D'Adamo, 1996).

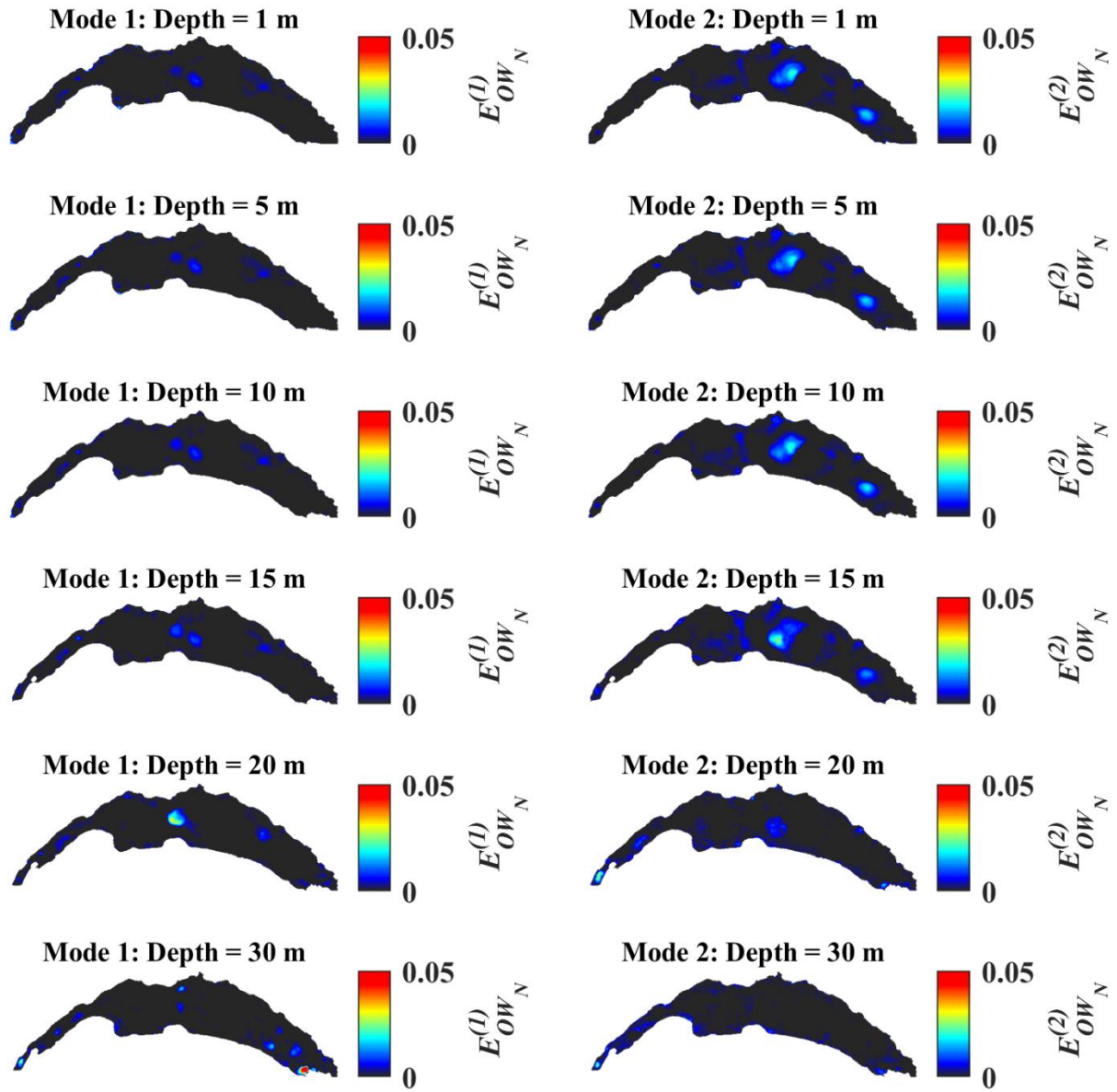


**Figure S2.** Empirical Orthogonal Function (EOF) analysis of the MITgcm output for Lake Geneva for September 2018. Shown are the positive values. Compare to Figure 3 in the main text where results for negative values are presented and indicate the presence of gyres. Colorbars give the EOF range.

35

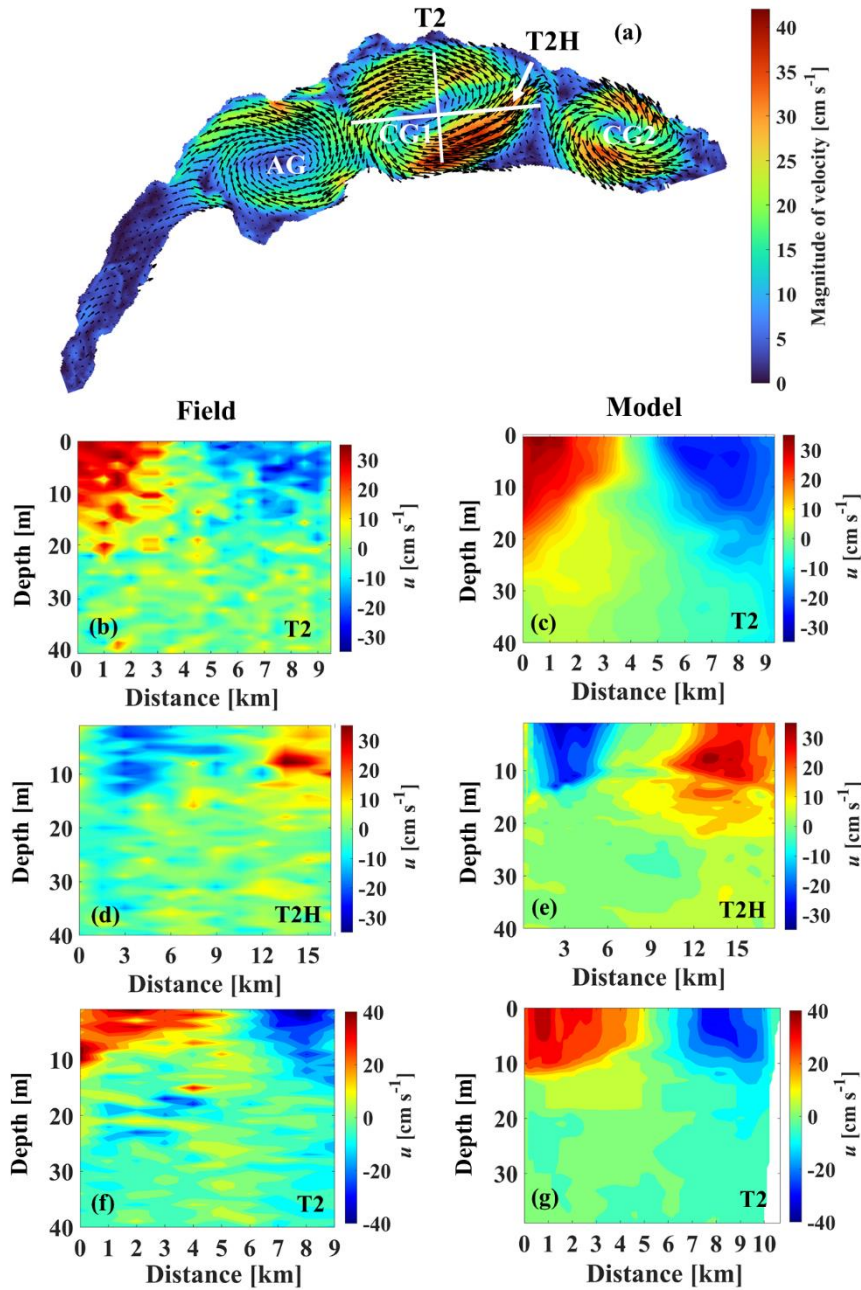
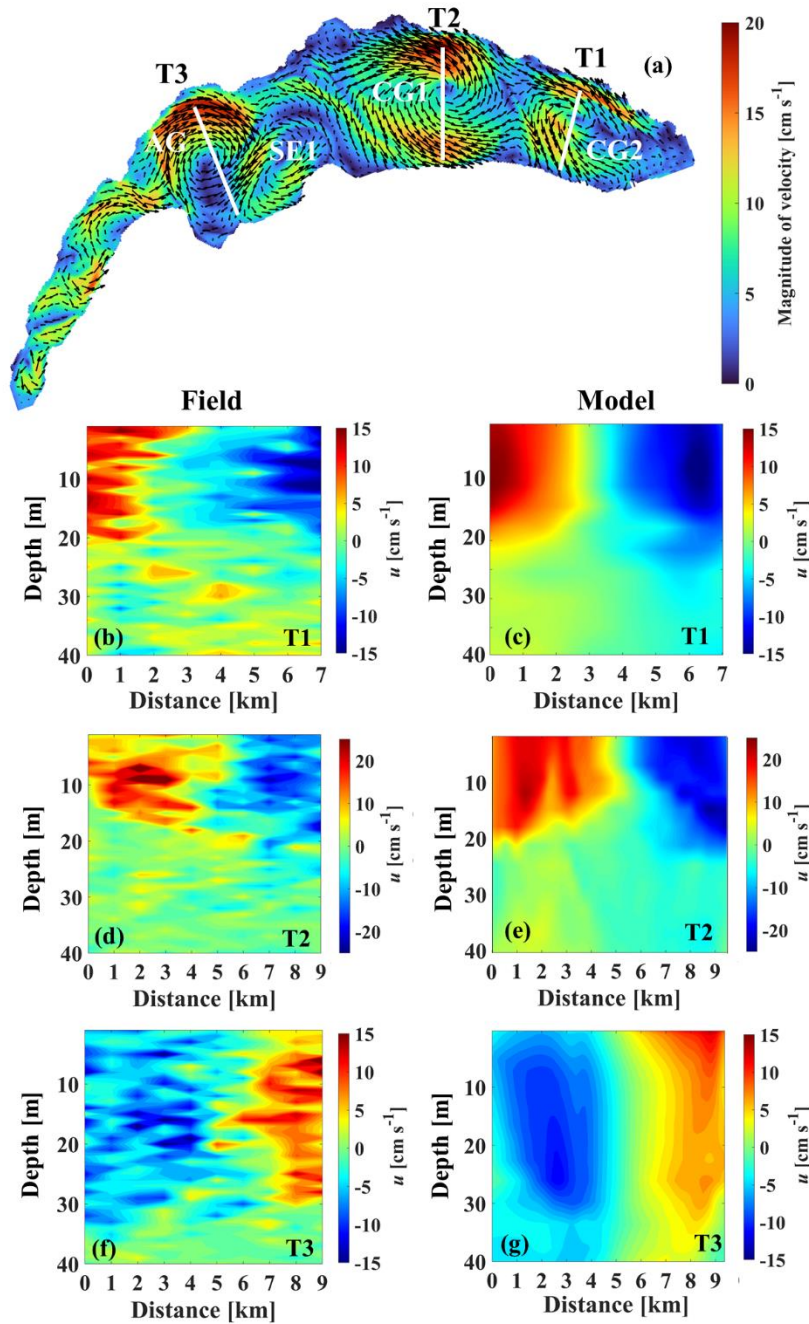
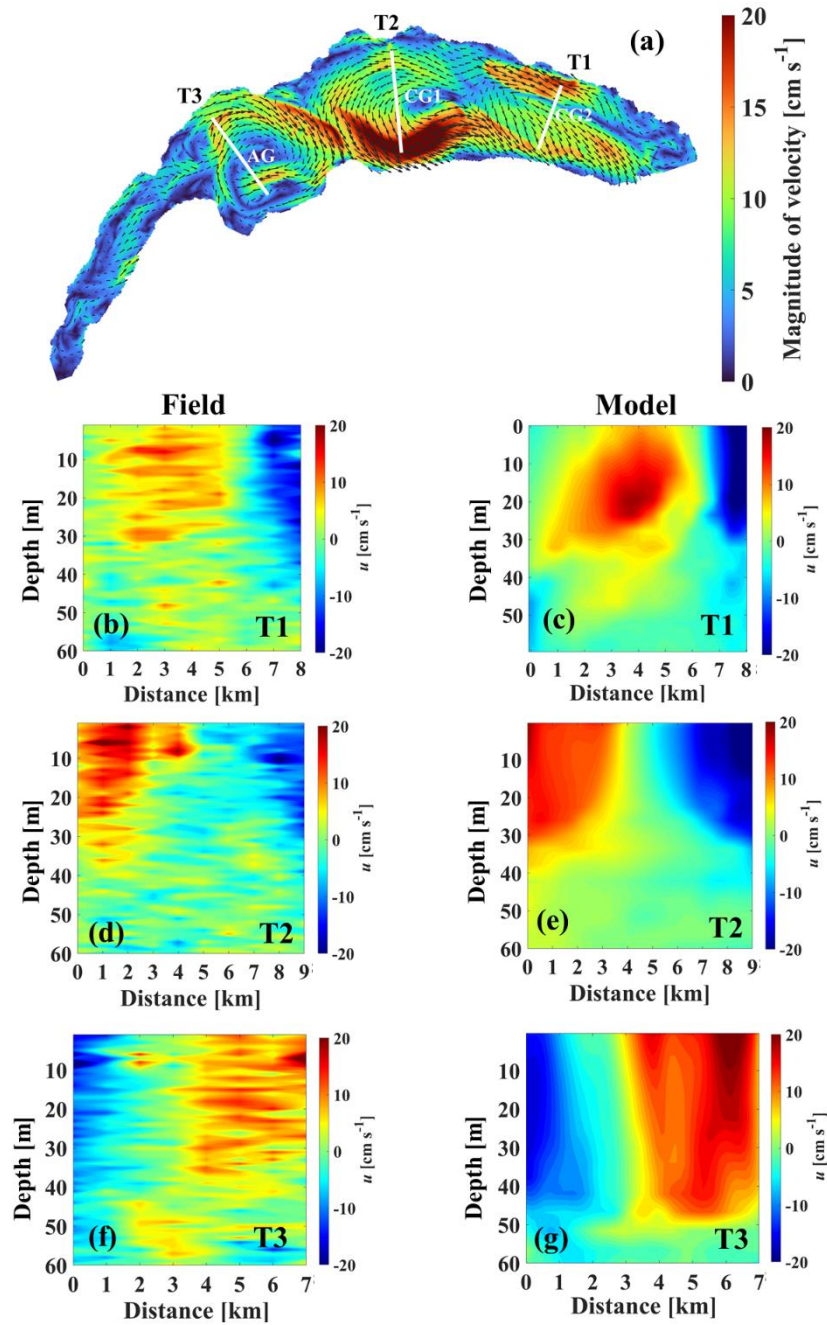


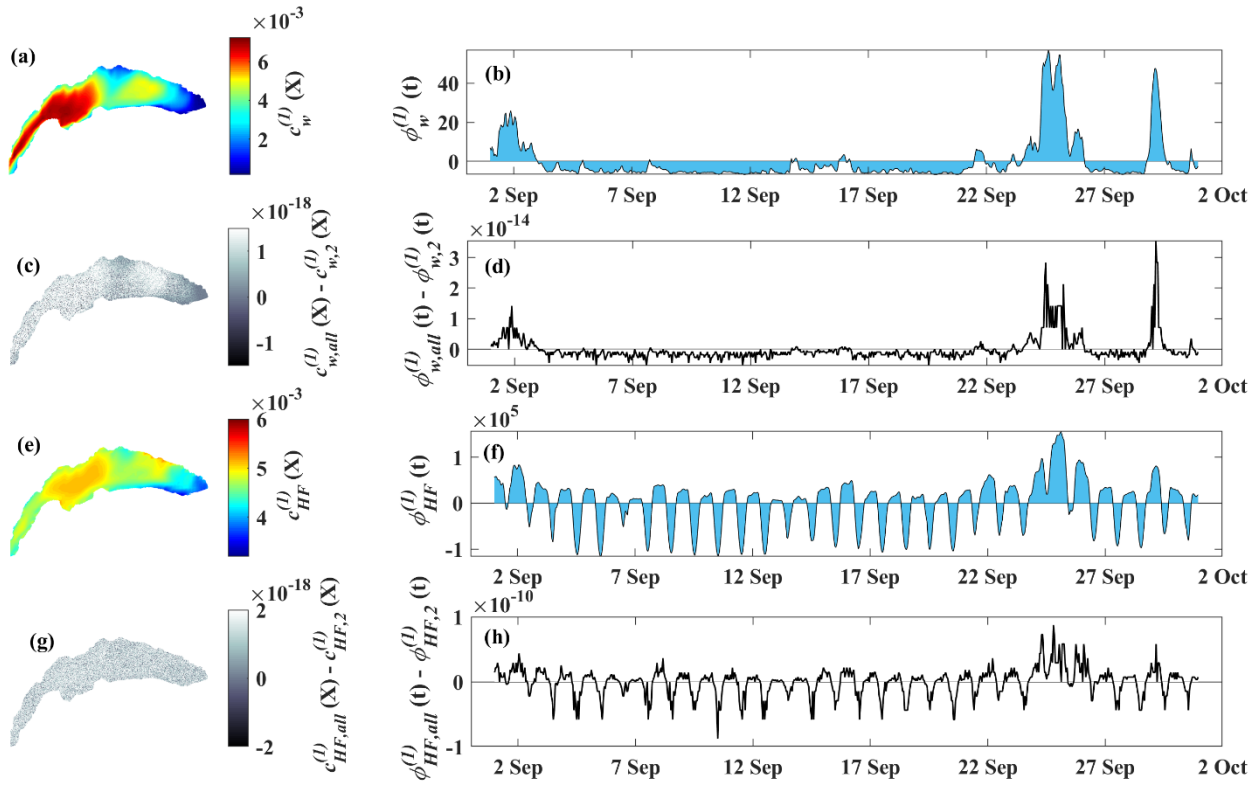
**Figure S3.** (a) Modeled surface velocity fields of the three-gyre (AG, CG1, CG2) pattern for 20 September 2019. Left column: Contour plot of field-measured horizontal velocity. Right column: corresponding modeled horizontal velocity contour plot. Plots (a) and (b) are for 20 September 2019 along Transect T2; (d) and (e) 22 September 2019 along T2H; (f) and (g) 22 September 2019 along T2. The colorbars indicate the horizontal velocity in  $\text{cm s}^{-1}$ . Positive velocities are pointing eastward for transect, T2, and northward for transect T2H.



45 **Figure S4.** (a) Modeled surface velocity fields of the three-gyre (AG, CG1, CG2) pattern for 24 October 2019. Black arrows show sense of rotation. Left column: Contour plot of field measured horizontal velocity. Right column: corresponding modeled horizontal velocity contour plot. Plots (a) and (b) are for 25 October 2019 along Transect T1; (d) and (e) for 24 October 2019 along T2; (f) and (g) for 24 October 2019 along T3. The colorbars indicate horizontal velocity. Positive velocities are pointing eastward. SE1 is a small eddy caught between gyres AG and CG1.



50 **Figure S5.** (a) Modeled surface velocity fields of three-gyre (AG, CG1, CG2) pattern for 25 November 2019. Black arrows show sense of rotation. Left column: Contour plot of field measured horizontal velocity. Right column: corresponding modeled horizontal velocity contour plot. Plots (b) and (c) present transect T1 measurements; (d) and (e) T2; (f) and (g) T3. The colorbars indicate horizontal velocity. Positive velocities point eastwards.



55 **Figure S6.** EOF analysis for September 2018 (a) First spatial mode and (b) principal component time series of the total wind  
 stress ( $\sqrt{\tau_x^2 + \tau_y^2}$ ) calculated from COSMO atmospheric data; (c) first spatial modes and (d) principal component time series  
 of noise between the solution with two dominant modes and the solution with all possible modes; (e) first spatial mode and  
 (f) principal component time series of the net upward heat flux during September 2018; (g) first spatial mode and (h)  
 60 principal component time series of noise between the solution with two dominant modes and the solution with all possible  
 modes for the net heat flux. The colorbars indicate the range of the parameters.

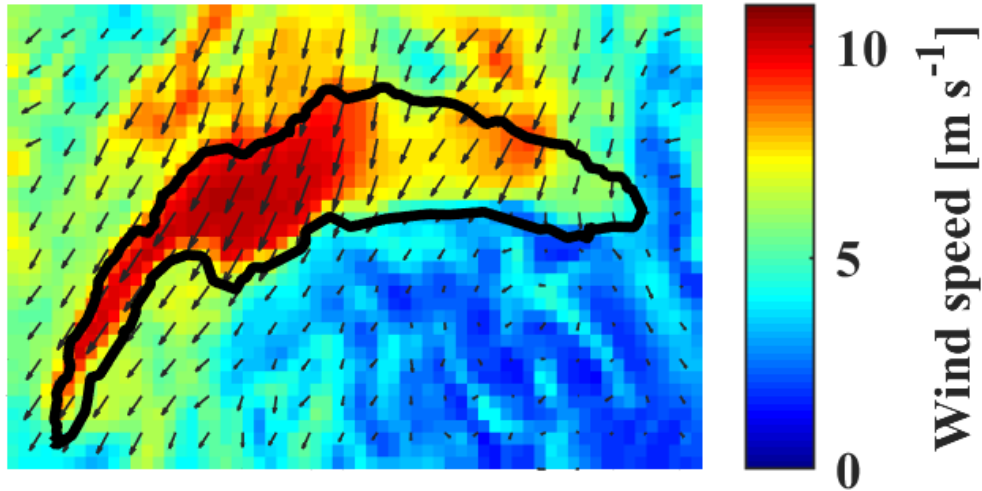


**Figure S7.** (a) Averaged wind speed (see colorbar for magnitudes) and direction (arrows) extracted from COSMO data during the *Bise* event that lasted from 24 to 26 September 2018.

#### **Text S2: EOF analysis for the October and November 2019 campaigns**

The first mode of the Empirical Orthogonal Function (EOF) analyses and the corresponding principal component time series for  $OW_N$  at 10-m depth and the first mode of the EOF analyses of wind stress for October and November 2019 are displayed in Figure S9. Patterns similar to those observed for September 2019 (Figure S8), with the three main gyres (AG, CG1, and CG2), are evident in the first mode of the EOF results for November 2019. The principal component time series corresponding to the spatial pattern for October 2019 indicates that the amplitude of the vorticity-dominated regime suddenly increased a few hours after the *Bise* event (marked by vertical green lines) started to decrease, whereas the amplitude of the vorticity-dominated regime for the November event gradually increased after the first peak of wind stress. The vorticity-dominated signature in the center of the lake persisted for almost 7 d after the *Bise* event until a strong *Vent* wind coming from the opposite direction started (Figure S9). The *Bise* wind pattern was approximately the same as that observed in September 2018 (Figure 5). However, the zones where the maximum wind stress is concentrated are at different locations. During October and November 2019, the maximum wind stress was observed near the center of the lake, whereas it was mainly concentrated on the western part of lake, i.e., the *Petit Lac* basin, in September 2019 (Figure S8).

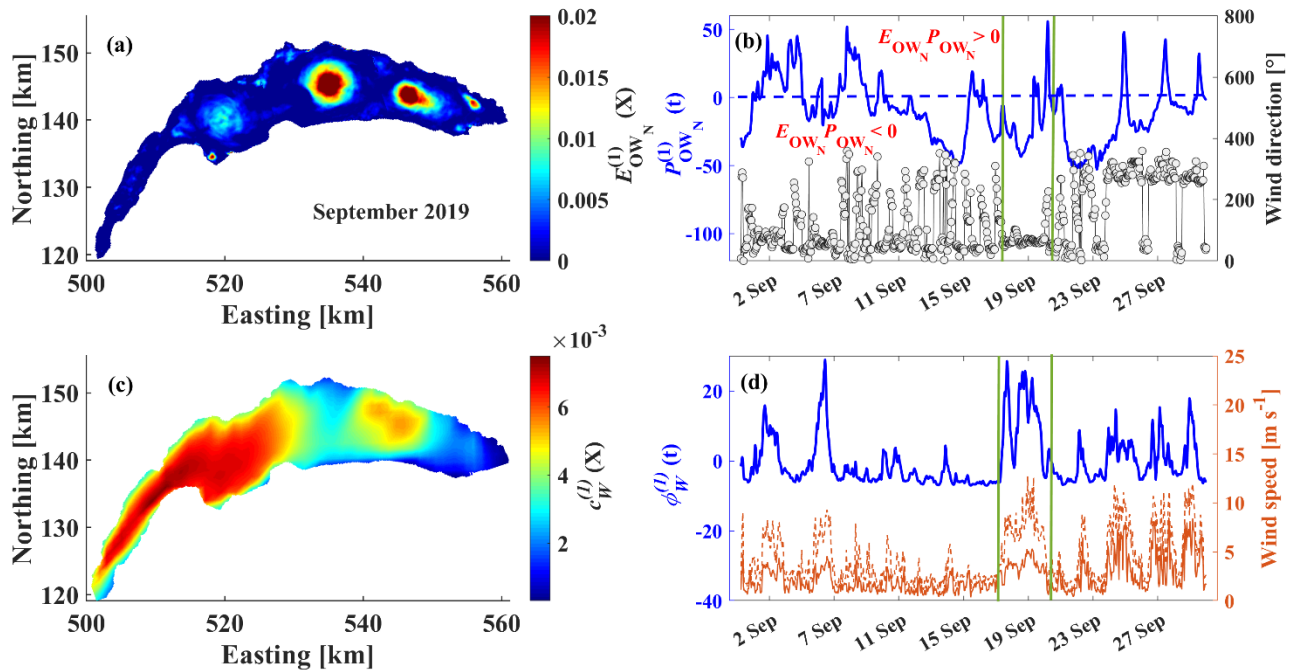


**Figure S8.** EOF analysis for September 2019: (a) first spatial mode and (b) top: principal component time series of the normalized Okubo-Weiss (OW<sub>N</sub>) parameter at 10-m depth (blue) and bottom: wind direction measured at the Buchillon station (black circles; for location, see Figure 1b); (c) first spatial mode and (d) top: the principal component time series of total wind stress ( $\sqrt{\tau_x^2 + \tau_y^2}$ ) calculated from the COSMO atmospheric data (blue) and bottom: wind speed measured at the Buchillon station (brown). The first mode in (a) is dominated by the three large-scale gyres (circular zones of negative OW<sub>N</sub> values, i.e.,  $E_{OW_N}(X)P_{OW_N}(t) < 0$ ). The colorbars indicate the parameter ranges. The vertical green lines mark the duration of the *Bise* wind event.

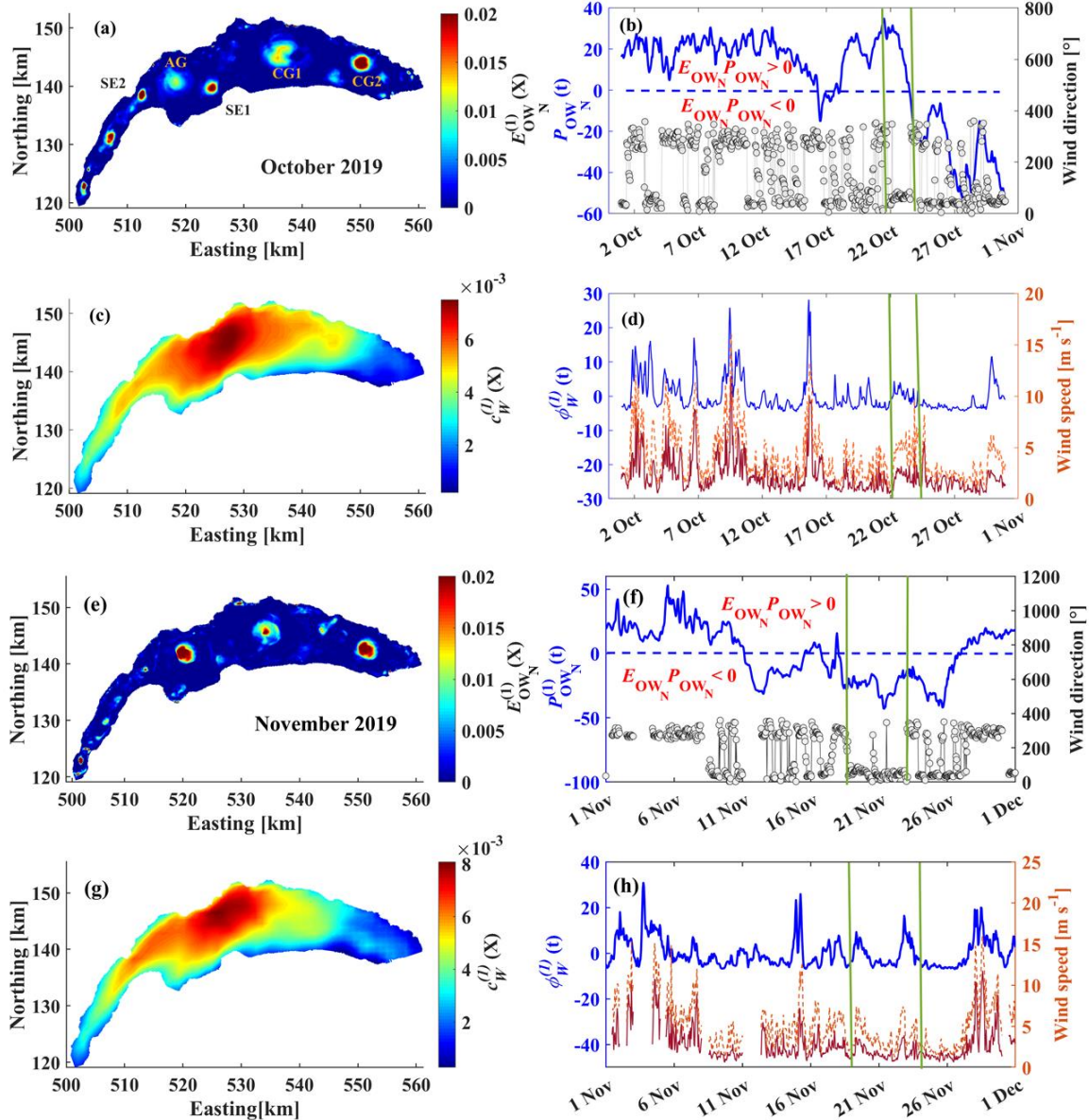


**Figure S9.** EOF analysis results. (a) First spatial mode and (b) top: principal component time series of the normalized Okubo-Weiss ( $OW_N$ ) parameter at 10-m depth (blue) and bottom: wind direction measured at the Buchillon station (black circles; for location, see Figure 1b) for October 2019. (c) First spatial mode and (d) top: corresponding principal component time series of the total wind stress ( $\sqrt{\tau_x^2 + \tau_y^2}$ ) calculated from COSMO atmospheric  $\tau$  data (blue) and bottom: wind speed measured at the Buchillon station (black circles) during October 2019. (e) First spatial mode and (f) top: principal component time series of  $OW_N$  at 10-m depth for November 2019 (blue) and bottom: wind direction measured at the Buchillon station (black circles). (g) First spatial mode and (h) top: corresponding principal component time series of the total wind stress (blue) and bottom: wind speed measured at the Buchillon station during November 2019 (brown). Negative  $E_{OW_N}P_{OW_N}$  values indicate the presence of large-scale gyres and mesoscale eddies. The colorbars give the range of the parameters. The vertical green lines mark the duration of the *Bise* wind event.

## References

- 95 Cushman-Roisin, B., and Beckers, J. M.: Introduction to Geophysical Fluid Dynamics: Physical and Numerical Aspects, Academic Press, TS15: <https://doi.org/10.1016/B978-0-12-088759-0.00015-8>, 2011.
- Dokken, S. T., and Wahl, T.: Observations of spiral eddies along the Norwegian Coast in ERS SAR images, <http://hdl.handle.net/20.500.12242/1449> (last accessed 12 December 2022), 1996.
- Donelan, M. A., and Pierson Jr, W. J.: Radar scattering and equilibrium ranges in wind-generated waves with application to scatterometry, *J. Geophys. Res.: Oceans*, 92(C5), 4971-5029, <https://doi.org/10.1029/JC092iC05p04971>, 1987.
- 100 Johannessen, J. A., Kudryavtsev, V., Akimov, D., Eldevik, T., Winther, N., and Chapron, B.: On radar imaging of current features: 2. Mesoscale eddy and current front detection, *J. Geophys. Res.: Oceans*, 110(C7), C07017, <https://doi.org/10.1029/2004JC002802>, 2005.
- Johannessen, J. A., Shuchman, R. A., Digranes, G., Lyzenga, D. R., Wackerman, C., Johannessen, O. M., and Vachon, P. W.: Coastal ocean fronts and eddies imaged with ERS 1 synthetic aperture radar. *J. Geophys. Res.: Oceans*, 101(C3), 6651-6667, <https://doi.org/10.1029/95JC02962>, 1996.
- 105 Karimova, S.: Spiral eddies in the Baltic, Black and Caspian seas as seen by satellite radar data, *Adv. Space Res.*, 50(8), 1107-1124, <https://doi.org/10.1016/j.asr.2011.10.027>, 2012.
- Lemmin, U., and D'Adamo, N.: Summertime winds and direct cyclonic circulation: Observations from Lake Geneva, *Ann. Geophys.*, 14(11), 1207-1220, <https://doi.org/10.1007/s00585-996-1207-z>, 1996.
- 110 Moran, M. S., Hymer, D. C., Qi, J., and Kerr, Y.: Comparison of ERS-2 SAR and Landsat TM imagery for monitoring agricultural crop and soil conditions, *Remote Sens. Environ.*, 79(2-3), 243-252, [https://doi.org/10.1016/S0034-4257\(01\)00276-0](https://doi.org/10.1016/S0034-4257(01)00276-0), 2002.
- Wang, C., Tandeo, P., Mouche, A., Stopa, J.E., Gressani, V., Longepe, N., Vandemark, D., Foster, R.C., and Chapron, B.: Classification of the global Sentinel-1 SAR vignettes for ocean surface process studies, *Remote Sens. Environ.*, 234, 111457, <https://doi.org/10.1016/j.rse.2019.111457>, 2019.
- 115 Yamaguchi, S., and Kawamura, H.: SAR-imaged spiral eddies in Mutsu Bay and their dynamic and kinematic models, *J. Oceanogr.*, 65(4), 525-539, <https://doi.org/10.1007/s10872-009-0045-5>, 2009.